

# A Novel Sidewinding Snake Robot with Non-zero Slope in Granular Terrains Modeled by DRFM

Lei Huang, *Student Member, IEEE*  
Dept. of Mechanical Engineering  
Shanghai Jiao Tong University  
Shanghai, China  
hl\_18sjtu@sjtu.edu.cn

Hengqiang Ming  
Dept. of Mechanical Engineering  
Shanghai Jiao Tong University  
Shanghai, China  
1362525207@sjtu.edu.cn

Yuehong Yin\*, *Member, IEEE*  
Dept. of Mechanical Engineering  
Shanghai Jiao Tong University  
Shanghai, China  
yhyin@sjtu.edu.cn

**Abstract**—Exploring granular terrains like loose sand is usually not easy for robots, which must solve the sinking and low-moving efficiency problems. Relying on a unique sidewinding gait, snakes can move efficiently in granular terrains, which brings design insight for continuum robots. However, most previous studies of snake-like sidewinding robots focus on the lateral undulation motion like a sine wave, but few generate the body's non-zero slope like real snakes. In this article, we analyze the effect of non-zero slope on locomotion efficiency using a Dynamic Resistive Force Model (DRFM) and a material point method (MPM). This work develops a non-wheeled 3D printed snake robot, and the body's slope can be changed. In addition, the unique structure with soft helix rod makes it have more than 35 degrees of freedom in 35 centimeters in length. In order to reduce weight and complexity, the robot needs only a single motor to achieve the sidewinding gait. Experiments not only confirm that the robot can move more efficiently by changing the slope, which shows the importance of the non-zero slope of the snake robot but demonstrates the designed robot's ability to explore in granular terrains.

**Index Terms**—Biologically-inspired robots, field robots, methods and tools for robot system design, biomimetics

## I. INTRODUCTION

The task of searching and roaming in granular terrains is not easy for robots [1]. One such example is that NASA's Mars rover Spirit got stuck in sulfate in 2009, leading to the end of the mission [2]. In nature, snakes have unique muscle tissues and bones, which enable them to be competent for various terrain with different gaits [3]. Typical snake-like locomotion includes the following types of gait, sidewinding, lateral undulation, accordion, linear movement, etc [4], [5]. In the granular terrain represented by dunes, the snake lifts its body segments off the ground at the same slope angle in turn to form a sidewinding gait and presents a locomotion track of diagonal travel on the ground [3]. According to biologists, compared with other gaits, sidewinding on hard ground has significant energy advantages [6], [7]. The sidewinding gait of snakes in granular terrain has the following advantages. First of all, the sidewinding gait of the snake is stable because it has many different contact areas with the ground in each gait cycle [8]. Second, the snake's locomotion has a high degree of redundancy because its body has a lot of repeated redundancy [9]. Third, in the sidewinding gait, the snake only needs to lift its body slightly, which consumes less energy than other snake-



Fig. 1. An overview of the snake robot locomotion experiment. The snake robot is moving on granular terrain. The robot is driven by a single dc motor to generate sidewinding locomotion. The motion data is captured by the motion capture system through five reflective markers on the snake robot.

like gaits [3]. These advantages may bring biological design inspiration to robots. However, most of the dynamic analysis of sidewinding is based on the hard ground [6], [10]–[12], and only a few studies have carried out the kinematic analysis of sidewinding in granular terrain [4], [13]. It is still necessary to analyze the dynamics of sidewinding in granular terrain so as to facilitate the integration of sidewinding in robots and realize the locomotion in granular terrain.

In view of the diversity and advantages of snakes' gait, more and more researchers have developed robots inspired by snake locomotion. Traditionally, snake-like robots imitate the cervical spine of snakes by connecting rigid links [14]. Some robots realize sidewinding by generating lateral waves [15], [16], while others generate linear propulsion through complex structures [17], [18]. Biologists found the asymmetric lift caused by the non-zero slope of the snake body by analyzing the data of the sidewinding gait of the snake [3], [19]–[21], and Zhang *et al.* proved the importance of this asymmetric lift for sidewinding [12]. However, only a few robots have noticed this feature, and most robots only focus on the sine wave locomotion in the horizontal plane. Hamidreza *et al.* designed a CMU robot. Each module uses two motors to realize the locomotion in the horizontal and vertical planes [13]. However, this kind of robot is still too heavy, limited by the material and drive, so it is challenging to design a robot with the same size and equivalent degree of freedom as a real snake.

In order to make up for the above shortcomings, we first use a Dynamic Resistive Force Model (DRFM) based on Granular Resistive Force Theory (RFT) to analyze the sidewinding

gait in granular terrain [22], [23]. DRFM expands RFT to the three-dimensional situation, so it is suitable to analyze the sidewinding gait, which is a three-dimensional intrusion scene. A material point method (MPM) is used to consider the local terrain damage influence. Further, the influence of non-zero slope angle on the sidewinding in granular terrain is analyzed. On this basis, we propose a continuous wheelless snake-like robot with a single motor. The robot has a novel helix structure which makes the robot have more than 35 degrees in 35 centimeters. The robot can not only achieve efficient sidewinding gait through the single motor rotation but also keeps a lightweight [see Fig. 1].

This paper is organized as follows. In sections II, the works related to the mechanical analysis model and material point method are introduced. In sections III, the Dynamic Resistive Force Model is used to analyze the influence of non-zero slope on the sidewinding locomotion in granular terrain. In sections IV introduces the robot design and kinematics model, and the effectiveness of the robot sidewinding in granular terrain is verified by experiments. The material point method is used to analyze the local terrain damage influence and corrects the DRFM predicted results. Finally, the advantages, limitations, and potential applications of robots are discussed.

## II. RELATED WORK

### A. Mechanical Analysis Method

The terramechanics analysis method is the basis for designing robots applied in granular terrain. The traditional method is calibrating specific granular parameters through plenty of experiments and then conducting mechanical analysis [24]–[27]. However, these methods are design-independent, so it is still a challenge to obtain design guidance through theoretical analysis.

The recently proposed Granular Resistive Force Theory (RFT) has shown impressive results in many granular tests [22], [28]. RFT extends the Fluid Resistive Theory to granular

and directly establishes the relationship between micro-surface and intrusion force, which can be expressed as:

$$F = \int (dF_{\perp} + dF_{\parallel}) = \int ds [f_{\perp}(v, \hat{t}) \hat{n} + f_{\parallel}(v, \hat{t}) \hat{t}] \quad (1)$$

where the function forms of  $f_{\perp}$  and  $f_{\parallel}$  can be solved from Stokes equations, but the analytical solution is not easy to obtain. The current research has experimentally calibrated two different forms: horizontal and vertical intrusion [see Fig. 2].

However, RFT is still unable to solve the general three-dimensional intrusion problem. We have proposed a Dynamic Resistive Force Model (DRFM), which extends RFT to a three-dimensional form smoothly, and additional velocity terms make the model suitable for dynamic intrusion [23]. Experiments have proved that DRFM has a high prediction accuracy, so it is suitable for analyzing the sidewinding dynamics of snakes in granular terrain in principle.

### B. Simulation Analysis Method

Although DRFM can accurately perform mechanical analysis, it cannot capture local terrain damage caused by locomotion. In order to solve this problem, the interaction between the robot and the terrain can be accurately simulated by the numerical simulation method. The traditional methods include the discrete element method (DEM) and finite element method (FEM) [29]–[31]. DEM is a particle-based simulation method. Compared with grid-based FEM, it can accurately simulate the interaction between the robot and granular terrain through a reasonable contact model and constitutive relationship with appropriate discretization analysis [30]. However, the particle-based simulation still has the problems of high computing cost and non-convergence.

Different from the previous methods, the material point method (MPM) has both the speed advantage of grid-based simulation and the high accuracy of particle-based simulation [32], [33]. According to the research of Klar *et al.* [34], we establish an MPM suitable for granular terrain simulation based on Taichi Lang, and the MPM stages are shown in Fig. 3. The APIC method is used to reduce the computing cost [35], and the stress projection algorithm is used to deal with non-associative flow. Taichi Lang is an open-source, parallel

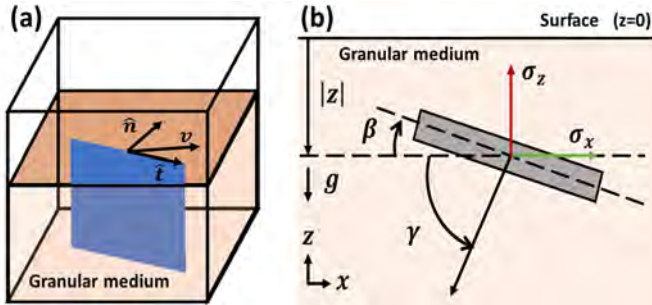


Fig. 2. **RFT model.** (A) RFT model in the horizontal plane. The intrusion force is related to the angle  $\psi$ , defined as the angle between the direction of  $v$  and the tangential direction  $\hat{t}$  [28]. (B) RFT model in the vertical plane. The lift stress  $\sigma_z$  and drag stress  $\sigma_x$  are determined by depth  $|z|$ , attack angle  $\beta$  and intrusion angle  $\gamma$  [22].

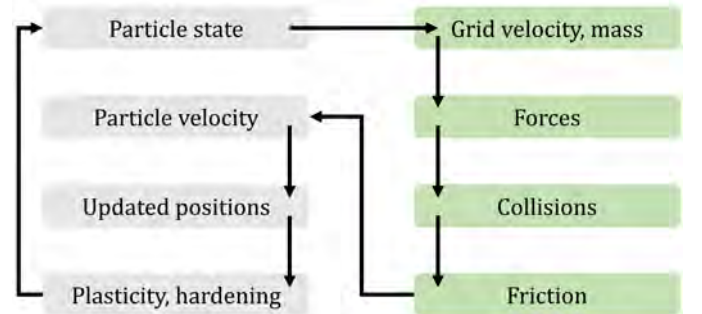


Fig. 3. **An overview of MPM stages.** The granular particle states (mass and momentum) are transferred to the grid by using APIC [35].

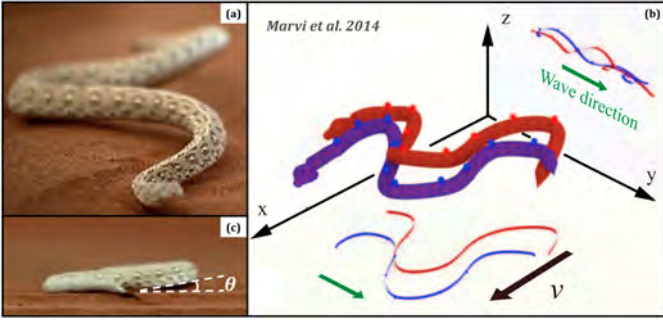


Fig. 4. **Snake sidewinding locomotion on granular media.** (A) A sidewinding rattlesnake locomoting on sand terrain. (B) Snake motion capture data shows that sidewinding not only generates sine waves in the horizontal ( $xy$ ) plane but also generates waves with the same period but smaller amplitude in the vertical ( $yz$ ) plane. [13]. (C) The angle between the snake body and the ground is defined as  $\theta$ .

programming language for high-performance numerical computation, which further improves the simulation speed [36]. We use the established MPM to analyze the influence of local terrain damage caused by sidewinding locomotion on dynamics.

### III. SIDEWINDING LOCOMOTION ANALYSIS

#### A. Sidewinding Kinematics Analysis

The sidewinding locomotion of a snake is generated by the mutual cooperation of muscles and bones rather than a simple plane sine wave. As shown in Fig. 4(b), biologists find through the motion capture system that sidewinding not only generates backward propagating waves in the horizontal ( $xy$ ) plane but also generates waves with the same period but smaller amplitude in the vertical ( $yz$ ) plane [13]. Tingle *et al.* have recorded the kinematic data of rattlesnakes and open source them, and similar phenomena can be observed [37].

According to Marvi *et al.* [13], the phase difference between the waves in the  $xy$  and  $yz$  plane is tiny ( $<1/4T$ ), so the waves of snake body in  $xy$  and  $yz$  planes can be modeled as:  $\kappa_1(s, t) = \epsilon_1 \cos(2\pi k(s + t))$  and  $\kappa_2(s, t) = \epsilon_2 \cos(2\pi k(s + t))$ , where  $\epsilon$ ,  $k$ ,  $s$ , and  $t$  represent amplitude, wavenumber, arc-length, and time, respectively. From the side view, the snake seems to be moving in a plane that forms an angle with the ground [see Fig. 4(c)]. We define this angle  $\theta$  as the slope angle.

#### B. Sidewinding Dynamics Analysis

Next, we introduce how to use DRFM to analyze snake sidewinding dynamics. We use the previously proposed DRFM to analyze sidewinding locomotion [23]. As shown in Fig. 5,  $E_i$  is the world frame, where  $E_2$  defines the snake moving direction, and  $E_3$  defines the vertical axis. The snake skin is discretized into numerous micro-surfaces, and the local frame of each micro-surface is established and defined by DRFM.  $e_i$  is a local frame fixed on a micro-surface, where  $e_2$  lies in the plane formed by the normal vector  $\hat{n}$  of surface and the vertical axis  $e_3$ , and  $e_1$  is obtained by the cross multiplication by  $e_2$  and  $e_3$ .

#### Algorithm 1 Snake Sidewinding Dynamics Analysis.

---

**Require:**  $\zeta$ ,  $C$ ,  $\gamma_0$  and  $\rho_c$  {RFT and material parameters};  
**Ensure:**  $\mathcal{D}$  {dynamics parameter};

- 1: discretize snakeskin  $S$  into sub-surfaces  $\{s_1, s_2 \dots s_m\}$ ;
- 2: Initialize  $\mathcal{D} \leftarrow 0$  {dynamics parameters}
- 3: **repeat**
- 4:   compute  $z$ ,  $v$ ,  $ds$ ,  $\hat{n}$ ,  $\gamma$ ,  $\beta$ ,  $f_1$  and  $f_2$  for each sub-elements ( $s_i$ )
- 5:   compute the force ( $F_i$ ) for each  $s_i$  by using DRFM
- 6:   compute the total force:  $F = \sum f_i$
- 7:   update  $\mathcal{D}$ ;
- 8:    $T_{i+1} = T_i + \Delta t$
- 9: **until**  $T_i \geq T_s$

---

According to DRFM, the angle between  $\hat{n}$  and  $e_2$  is defined as  $\beta - 90^\circ$ ; The velocity  $v$  of the micro-surface is decomposed into  $v_1$  and  $v_{23}$ , where  $v_1$  is along the direction of  $e_1$ , and  $e_{23}$  represents the direction of  $v_{23}$ . This micro-surface generates forces in two directions: In the  $e_1$  direction,  $F_1$  is generated caused by flow resistance. In the  $e_2$ - $e_3$  plane,  $F_{23}$  is generated, which is jointly affected by the yield stress and flow resistance of the granular media. The total force can be expressed as:

$$F = f_1(\hat{v}, \hat{e}_1)F_1 + f_2(\hat{v}, \hat{e}_{23})F_{23} \quad (2)$$

where

$$F_{23} = \int [-\alpha_x(\beta, \gamma)\hat{e}_2 + \alpha_z(\beta, \gamma)\hat{e}_3]|z|ds \quad (3)$$

$$F_1 = \int [-\alpha_x(0, 0)\hat{e}_1]|z|ds$$

where the coefficients ( $\alpha_z$  and  $\alpha_x$ ) denote intrusion stresses per unit depth in the vertical and horizontal direction, respectively. The coefficients are related to attack angle  $\beta$  and intrusion angle  $\gamma$  [see Fig. 2(b)]. Li *et al.* have proved that the coefficients  $\alpha_z$  and  $\alpha_x$  of most granular media have similar characteristics. Most granular media coefficients  $\alpha_{z,x}$  can be calculated by multiplying a scaling factor  $\zeta_i$  with a generic Fourier coefficient  $M_0$  [22].  $\zeta_i$  is determined by the resistance of specific granular media, and it can be calibrated by the vertical penetration test:

$$\zeta_i \approx 0.8\alpha_z(0, 90^\circ) \quad (4)$$

The scaling factor has the form:

$$f_1(\hat{v} \cdot \hat{e}_1) = \hat{v} \cdot \hat{e}_1$$

$$f_2(\hat{v}, \hat{e}_{23}) = (1 + \frac{C}{\sqrt{\tan^2 \gamma_0 + (\hat{v} \cdot \hat{e}_{23})^2}})(\hat{v} \cdot \hat{e}_{23}) \quad (5)$$

where the coefficient  $C$  is related to the yield stress and the flow resistance coefficient.  $\gamma_0$  is the internal slip angle.

The resistive force generated by intrusion speed has the form:

$$F_v = \int (-\lambda \rho_c v^2) \hat{v} ds_\perp \quad (6)$$



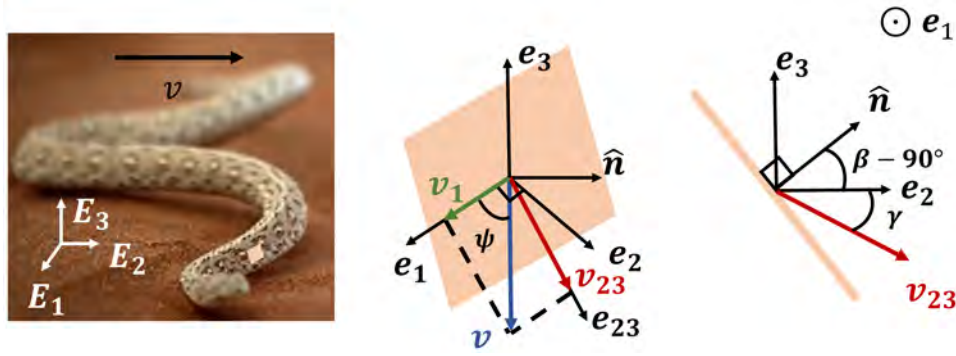


Fig. 5. **Using DRFM to analyze snake sidewinding dynamics.** The snake skin is discretized into micro-surfaces, and each surface is fixed with a local frame according to DRFM definitions. The green vector ( $v_1$ ) indicates the projection of velocity in the  $e_1$  direction, and the red vector ( $v_{23}$ ) indicates the projection in the  $e_2$ - $e_3$  plane. In the view of  $e_1$  axis,  $\beta$  and  $\gamma$  are defined by  $v_{23}$  and  $\hat{n}$  as presented in Fig. 2.

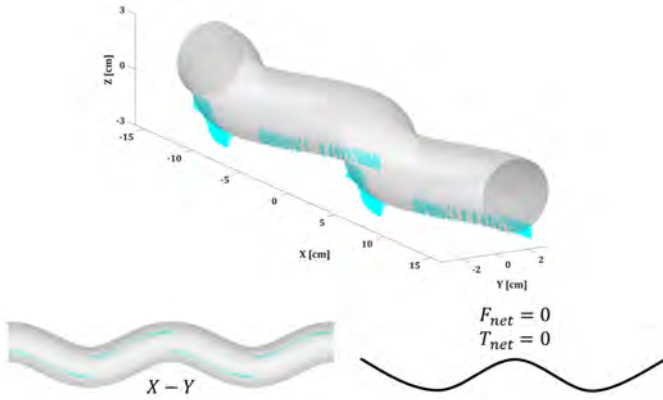


Fig. 6. **Zero slope angle sidewinding.** The top shows the force analysis of the snake sidewinding with zero slope angle using DRFM. From the view of the  $X$ - $Y$  plane, the force is symmetrical, so the total net force and torque are zero, which leads to low sidewinding locomotion efficiency.

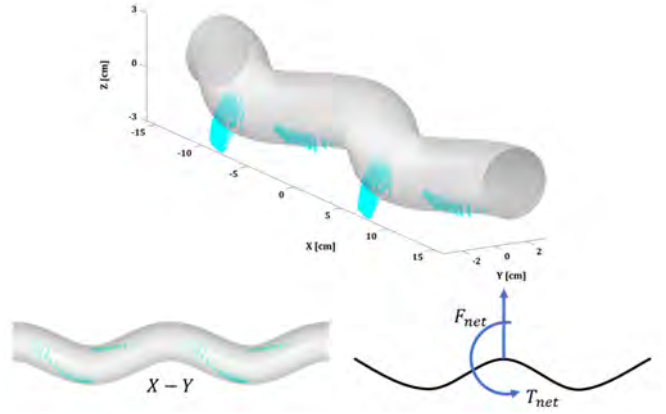


Fig. 7. **Non-zero slope angle sidewinding.** The top shows the force analysis of the snake sidewinding with a non-zero slope angle using DRFM. From the view of the  $X$ - $Y$  plane, the force is asymmetrical, so the total net force and torque are no longer zero, which pushes the snake forward.

where  $\rho_c$  is the effective granular media density,  $ds_{\perp}$  is the projection of the surface in a plane perpendicular to intrusion velocity  $v$ .  $\lambda$  is an  $O(1)$  scalar fitting constant.  $\hat{v}$  represents the direction of velocity. The total force of the surface, including speed influence, is:

$$F = f_1(\hat{v}, \hat{e}_1) \mathbf{F}_1 + f_2(\hat{v}, \hat{e}_{23}) \mathbf{F}_{23} + \int (-\lambda \rho_c v^2) \hat{v} ds_{\perp} \quad (7)$$

When the target dynamics parameter  $\mathcal{D}$  and the deadline  $T_s$  are set, the parameters can be updated through Algorithm 1.

### C. Slope Angle Analysis

Next, we analyze how the non-zero slope angle affects the sidewinding locomotion. The resultant force of snake sidewinding locomotion is set as the target dynamics parameter  $\mathcal{D}$ .

When the slope angle is zero ( $\beta = 0^\circ$ ), the snake is equivalent to generating a sine wave in the horizontal plane. The result is illustrated in Fig. 6. Since the sinusoidal locomotion is symmetrical, the force is also symmetrical. In this case, the net thrust is zero, so it cannot push the snake forward, which

is also why the snake-like robot considering only the plane fluctuation, has low locomotion efficiency.

When the slope angle is not zero ( $\beta = 15^\circ$ ), the result is illustrated in Fig. 7. It can be seen that the locomotion is asymmetric at this time, and a net thrust is generated in the direction of movement, thus pushing the snake forward.

The result shows that the non-zero slope is essential for the snake side movement, which is also required to produce a non-zero slope when designing the sidewinding snake robot.

## IV. METHOD AND EXPERIMENTS

### A. Robot Design

We have designed a continuous snake robot with a cylindrical helix rod, a continuous string of 3D-printed body shells, and a single rotary motor [see Fig. 8(f)]. In order to make the snake robot produce sidewinding locomotion, the snake robot should produce a larger amplitude sine wave in the horizontal plane and a smaller one in the vertical plane. We use the radial projection principle of the helix to generate an ideal sine curve and rotate the projection plane to generate sine curves with different amplitudes in both the horizontal and vertical

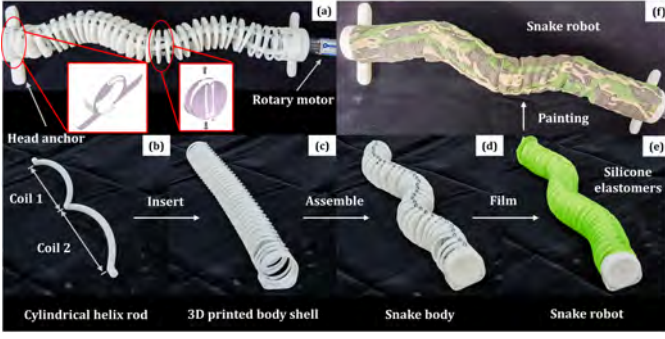


Fig. 8. **Fabrication of the continuous snake robot.** (A) The snake robot body with a single rotary motor. Different mounting holes on the head anchor are used to adjust the slope angle. The body shells are assembled by pins. (B) A cylindrical helix rod with two coils is made by 3D printing. (C) 3D-printed body shells are linked to form a robot snake shell. (D) The helix rod is put into the body shells to form the snake robot body. (E) The snake robot body is filmed with silicone elastomers to improve the friction coefficient. (F) Prototype of snake robot after painting.

planes. Moreover, a single rotary motor drives the helix rod to rotate around the central axis, thus generating a sine wave with continuous phase change. The specific manufacturing process is as follows:

*Step 1:* The cylindrical helix rod is made through 3D printing [see Fig. 8(b)], and the coils of the rod determine the number of the wave. The degrees of freedom can be further increased by using a spring helix rod similar to that of Zhao *et al.* [9].

*Step 2:* The body shell is made of photosensitive resin to ensure machining precision and reliability [see Fig. 8(c)]. The stereolithography appearance (SLA) technology is used to manufacture. The center of the shell is designed as a rectangular hole, wherein: the length of the long side is equal to the sum of the diameter of the cylindrical helix and the diameter of the helix rod; the length of the narrow side is equal to the diameter of the helix rod. Every two adjacent body shells are assembled by the upper and lower pins.

*Step 3:* Since the length of the narrow side of the central hole is equal to the diameter of the helix rod, a sine curve is formed in the direction of the narrow side. By contrast, the helix rod moves freely in the direction of the long side. After the assembly, the snake robot body results in a sine curve in a plane [see Fig. 8(d)].

*Step 4:* The snake robot body is filmed with silicone elastomers to improve the friction coefficient [see Fig. 8(e)], and the snake robot is painted after filming [see Fig. 8(f)]. The snake robot body is connected with the head anchors. The head anchor is used to change the slope angle of the snake robot, and different mounting holes on the head anchor can change the specific plane in which the sine curve lies [see Fig. 8(a)]. A single dc motor is fixed on the head anchor, and the rotary shaft is connected with the helix rod concentrically.

Fig. 8(f) shows the snake robot has a sine shape with a non-zero slope angle in the natural state. The parameters of the snake robot are listed in Table I. The effective length of the

TABLE I  
PARAMETERS OF THE SNAKE ROBOT

Parameters	Symbols	Values
Effective length of the snake robot <sup>a</sup>	$L$	35cm
Diameter of the body shell <sup>b</sup>	$D$	4cm
Helix angle of the helix rod	$\alpha$	60°
The coils of helix rod	$n$	2
Rotation speed of the motors	$\omega$	Variable
The slope angle of the snake robot	$\theta$	0°, 7.5°, 15°, 22.5°, 30°
DOFs of the robot		37
Totall weight of the robot		245g

<sup>a</sup> Length of the body shells in fully straightened state.

<sup>b</sup> Outer diameter of the body shells.

robot is 35cm, and the total length is 40cm (including 5cm of the motor). The outer diameter of the body shell is 4cm, which is close to the size of a real snake. The total weight of the snake robot is only 245g, which is lower than the previous study [9]. The robot has a total of 37 DOFs, more than 100 DOFs per meter of effective length. The snake robot is designed to have two sine waveforms. The amplitude of the sine waveform depends on the helix angle of the cylindrical helix rod. The larger the helix angle is, the smaller the waveform amplitude is. The dimension, DOFs, wave numbers, and amplitude of the snake robot can be easily customized by the cylindrical helix rod and body shell with different helix angles and dimensions. The rotation speed of the motor is variable to control the moving speed of the robot.

### B. Kinematics Modeling

The snake robot is actuated by a single dc motor to perform sidewinding locomotion. When the motor shaft rotates, the helix rod will also rotate relative to the body shells, resulting in wave-like locomotion of the robot [see Supplementary Movie S1].

The rotating twisted rod is abstracted into a helix curve, which can be described as follows:

$$\mathbf{r}(s, t) = \begin{cases} \frac{L \cos \alpha}{2\pi n} \cos(\frac{2\pi ns}{L} + \omega t) \\ s \sin \alpha \\ \frac{L \cos \alpha}{2\pi n} \sin(\frac{2\pi ns}{L} + \omega t) \end{cases} \quad (8)$$

where  $\mathbf{r}(s, t)$  is the coordinate of any point on the helix rod [see Fig. 8(b)],  $s$  is the arc length coordinate,  $t$  is the time, and other parameters have been listed in Table I.

Constrained by the body shells, the rotating twisted rod deforms into a traveling sine curve, which is a projection of the rotating helix curve onto the horizontal plane ( $xy$ ) and can be described by the following:

$$\kappa(s, t) = \frac{L \cos \alpha}{2\pi n} \cos(\frac{2\pi ns}{L} + \omega t) \quad (9)$$

When the plane of curve  $\kappa(s, t)$  rotates a slight angle  $\theta$ , the coordinate of any point on the curve can be described as following:

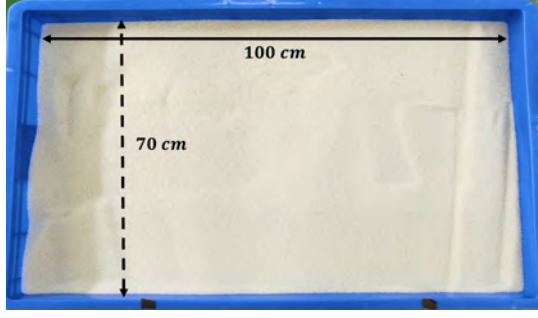


Fig. 9. **Snake robot locomotion experiments.** 0.8-1 mm glass beads are used as the substrate to fill a 100cm x 70cm x 15cm granular bed to 10 cm depth. According to our previous research [23], the coefficient  $C = 1.8$  and  $\gamma_0 = 13.8^\circ$  in (4) are considered.

$$\begin{aligned}\kappa_1(s, t) &= \frac{L \cos \alpha}{2\pi n} \cos\left(\frac{2\pi n s}{L} + \omega t\right) \cos \theta \\ \kappa_2(s, t) &= \frac{L \cos \alpha}{2\pi n} \cos\left(\frac{2\pi n s}{L} + \omega t\right) \sin \theta\end{aligned}\quad (10)$$

Since  $\theta$  is a slight angle,  $\sin \theta \sim \theta + O(\theta^3)$  and  $\cos \theta \sim 1 + O(\theta^2)$ . Then, the curve  $\kappa_1(s, t)$  and  $\kappa_2(s, t)$  can be represented as:

$$\begin{aligned}\kappa_1(s, t) &= \frac{L \cos \alpha}{2\pi n} \cos\left(\frac{2\pi n s}{L} + \omega t\right) \\ \kappa_2(s, t) &= \frac{L \theta \cos \alpha}{2\pi n} \cos\left(\frac{2\pi n s}{L} + \omega t\right)\end{aligned}\quad (11)$$

The sine wave is similar to the real snake shown in Fig. 4(b), which is consistent with the real snake sidewinding kinematic.

### C. Locomotion in Granular Terrain

To evaluate the performance of the snake robot in granular terrain, the snake sidewinding locomotion experiments were carried out in the granular bed. 0.8-1 mm glass beads were used as the substrate to fill a 100cm x 70cm x 15cm granular bed to 10 cm depth [see Fig. 9]. Reflective markers were placed on the body of the snake robot, and the kinematic data of the robot was captured by the motion capture system [see Fig. 1]. Eight motion capture cameras were mounted around the bed, and the kinematic data were captured by reflective markers attached to the robot at a speed of 60 frames per second.

We first explored the relationship between the slope angle and the moving speed. The slope angle between head anchors and body shell was set to  $0^\circ$ ,  $7.5^\circ$ ,  $15^\circ$ ,  $22.5^\circ$ , and  $30^\circ$ , respectively, and the rotation speed of the dc motor to  $1.5 r/s$ . The experimental data were collected after the robot reached a steady state, and each group of trials was tested more than four times. Between each trial, the granular bed was reset by manually scraping. When the slope angle was  $0^\circ$ , the snake robot failed to move, which was consistent with the theoretical analysis. When the slope angle was less than  $15^\circ$ , the moving speed of the snake robot increased with the increase of the slope angle and reached the maximum value between  $15^\circ$  and  $20^\circ$ .

DRFM with velocity term (7) was used to analyze this phenomenon. When the snake robot moved steadily, its resultant force was equal to zero. Therefore, let  $F$  in (7) equal zero, then the theoretical steady-state speed could be obtained [see Fig. 10]. On the other hand, the speed of the robot snake should be less than the projection component of the maximum wave fluctuating speed in the horizontal plane, that is:  $v \leq L\omega \cos \theta \cos \alpha / (2\pi n)$ . From the results, DRFM with the speed correction could accurately predict the moving speed further.

Next, we analyzed the relationship between the rotation speed and the snake robot's moving speed. The slope angle was set to  $15^\circ$ , and the rotation speed of the dc motor was set to 0.5, 1, 1.5, 2, 2.5,  $3r/s$ , respectively. Similarly, each group of trials was tested more than four times. We found that the robot snake reached its maximum speed at the rotation speed of around  $2r/s$  and nearly did not change with the increase of the speed. Through the observation, when the rotation speed was too high, the slip rate of the robot snake increased, resulting in a height difference between the free surface front and back of its moving direction. We used MPM to analyze this phenomenon. A cylinder with a diameter the same as the body shell of the snake robot was set to move at different speeds in MPM simulation, and the data  $\delta h$  were collected [see Fig. 11].

Since MPM involved many parameters, we analyzed the free surface variations for the specific granular material through dimensional analysis. The physical parameters that affected the free surface variations  $\delta h$ , including velocity ( $v$ ), gravitational acceleration ( $g$ ), and body shell diameter ( $D$ ). By dimensionless parameter, it suggested the form  $\delta h = r\psi(v^2/(rg))$  for

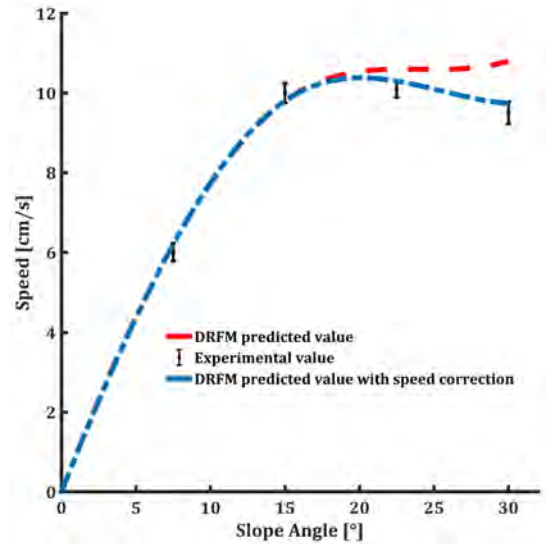


Fig. 10. **The Influence of slope angle on the moving speed of the snake robot.** Experimental measured data (black dots) represent means over four experimental trials. The error bar indicates  $\pm$  standard deviation of results. The red dotted line indicates the predicted speed value of DRFM without speed correction, while the blue dotted line indicates the predicted speed value of DRFM with speed correction.



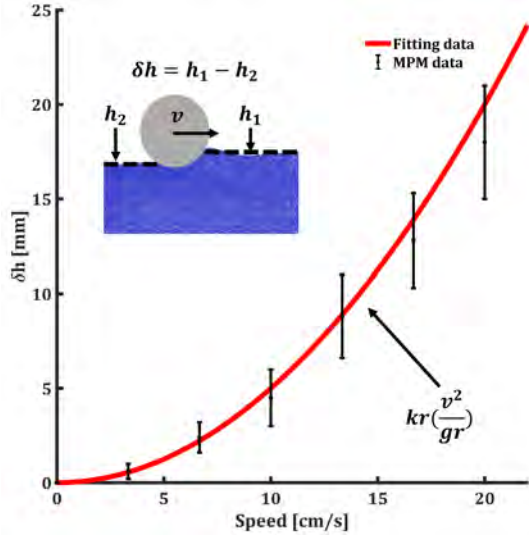


Fig. 11. The effective free surface variations during sidewinding locomotion.  $\delta h$  represents the gap between front ( $h_1$ ) and back ( $h_2$ ) free surface height. MPM data (black dots with error bars) and fitting line (red line) for  $\delta h$ .

some function  $\psi$ . By comparing with the experimental data, we found that  $\psi$  was well-approximated by a linear function. The fitting function had the form of  $\delta h = kr(v^2/(rg))$  [see Fig. 11].

Since the free surface variations were caused by local terrain damage, we called  $\delta h$  local terrain correction. We added  $\delta h$  to 3 to correct the depth  $z$  and used DRFM with  $\delta h$  correction to estimate the steady-state speed. The DRFM corrected with local terrain damage  $\delta h$  showed good agreement with the experimental results. The detail of the snake robot and model can be found through the open-source link: <https://github.com/sidewinding/snakerobot>.

## V. CONCLUSION

The kinematics model of snake sidewinding in granular terrain is illustrated in this article, and the dynamics are analyzed through DRFM. The results show that the non-zero slope angle is essential to snake sidewinding. Furthermore, a material point method is used to analyze the free surface variation caused by local terrain damage. Experiments prove that the DRFM-predicted results with speed and local terrain correction agree with the experiment results.

On this basis, the proposed biologically-inspired snake robot has a continuous slender wheelless structure, which can perform sidewinding locomotion like a real snake. This robot is only used a single dc motor, a cylindrical helix rod, and a string of 3D printed body shells to make it less than 250g. The moving speed of the robot can be adjusted by the rotation speed of the motor. The experiments show the sidewinding capability of the robot. The preliminary prototype of the snake robot is connected by wires in this article.

For future work, adding a steering structure and integrating a power supply can significantly improve the practicality of the

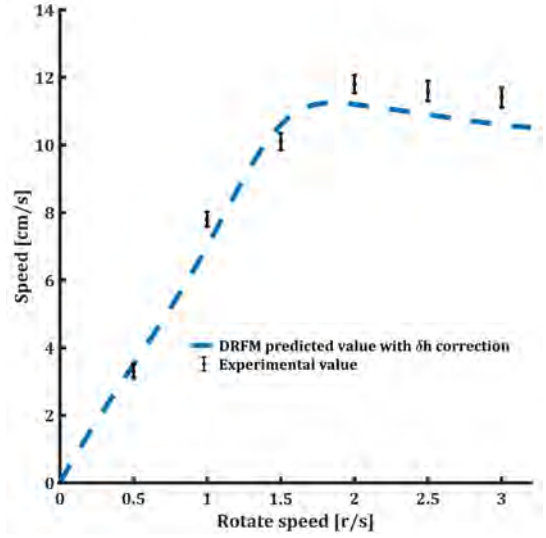


Fig. 12. The Influence of the motor's rotation speed on the moving speed of the snake robot. Experimental measured data (black dots) represent means over four experimental trials. The error bar indicates  $\pm$  standard deviation of results. The blue dotted line indicates the predicted speed value of DRFM with  $\delta h$  correction.

snake robot so that it can move more freely in various granular terrain. In addition, integrating more advanced sensors into the snake robot can be challenging but practical. For example, visual sensors will help improve the exploration ability. These above challenges will guide us to the next stage of our work.

This article reveals the biological mechanism of snake sidewinding locomotion in granular terrain, and the proposed snake robot has potential applications in desert exploration and rescue.

## REFERENCES

- [1] B. Schäfer, A. Gibbesch, R. Krenn, and B. Rebele, "Planetary rover mobility simulation on soft and uneven terrain," *Vehicle System Dynamics*, vol. 48, no. 1, pp. 149–169, 2010.
- [2] Arvidson, E. R., B. Iii, J. Bellutta, P. . Cabrol, N. Catalano, J. Cohen, J. . Crumpler, L. Marais, and D. Estlin, "Spirit mars rover mission: Overview and selected results from the northern home plate winter haven to the side of scamander crater," *Journal of Geophysical Research Planets*, vol. 115, no. E7, pp. 633–650, 2010.
- [3] J. Gray, "The mechanism of locomotion in snakes," *Journal of experimental biology*, vol. 23, no. 2, pp. 101–120, 1946.
- [4] B. C. Jayne, "Kinematics of terrestrial snake locomotion," *Copeia*, pp. 915–927, 1986.
- [5] S. J. Newman and B. C. Jayne, "Crawling without wiggling: muscular mechanisms and kinematics of rectilinear locomotion in boa constrictors," *Journal of Experimental Biology*, vol. 221, no. 4, p. jeb166199, 2018.
- [6] S. M. Secor, B. C. Jayne, and A. F. Bennett, "Locomotor performance and energetic cost of sidewinding by the snake *crotalus cerastes*," *Journal of experimental biology*, vol. 163, no. 1, pp. 1–14, 1992.
- [7] H. Marvi, J. Bridges, and D. L. Hu, "Snakes mimic earthworms: propulsion using rectilinear travelling waves," *The Royal Society*, no. 84, 2013.
- [8] R. L. Hatton and H. Choset, "Sidewinding on slopes," in *2010 IEEE International Conference on Robotics and Automation*. IEEE, 2010, pp. 691–696.
- [9] W. Zhao, J. Wang, and Y. Fei, "A multigait continuous flexible snake robot for locomotion in complex terrain," *IEEE/ASME Transactions on Mechatronics*, 2021.

- [10] W. Mosauer, "A note on the sidewinding locomotion of snakes," *The American Naturalist*, vol. 64, no. 691, pp. 179–183, 1930.
- [11] B. C. Jayne, "Muscular mechanisms of snake locomotion: an electromyographic study of lateral undulation of the florida banded water snake (*nerodia fasciata*) and the yellow rat snake (*elaphe obsoleta*)," *Journal of Morphology*, vol. 197, no. 2, pp. 159–181, 1988.
- [12] X. Zhang, N. Naughton, T. Parthasarathy, and M. Gazzola, "Friction modulation in limbless, three-dimensional gaits and heterogeneous terrains," *Nature communications*, vol. 12, no. 1, pp. 1–8, 2021.
- [13] H. Marvi, C. Gong, N. Gravish, H. Astley, M. Travers, R. L. Hatton, J. R. Mendelson III, H. Choset, D. L. Hu, and D. I. Goldman, "Sidewinding with minimal slip: Snake and robot ascent of sandy slopes," *Science*, vol. 346, no. 6206, pp. 224–229, 2014.
- [14] G. Miller, "13 snake robots for search and rescue," *Neurotechnology for Biomimetic Robots*, p. 271, 2002.
- [15] K. Osuka and H. Kitajima, "Development of mobile inspection robot for rescue activities: Moira," in *Proceedings 2003 IEEE/RSJ International Conference on Intelligent Robots and Systems (IROS 2003)(Cat. No. 03CH37453)*, vol. 4. IEEE, 2003, pp. 3373–3377.
- [16] A. Crespi, A. Badertscher, A. Guignard, and A. J. Ijspeert, "Amphibot i: an amphibious snake-like robot," *Robotics and Autonomous Systems*, vol. 50, no. 4, pp. 163–175, 2005.
- [17] K. A. Daltorio, A. S. Boxerbaum, A. D. Horschler, K. M. Shaw, H. J. Chiel, and R. D. Quinn, "Efficient worm-like locomotion: slip and control of soft-bodied peristaltic robots," *Bioinspiration & biomimetics*, vol. 8, no. 3, p. 035003, 2013.
- [18] A. Rafsanjani, Y. Zhang, B. Liu, S. M. Rubinstein, and K. Bertoldi, "Kirigami skins make a simple soft actuator crawl," *Science Robotics*, vol. 3, no. 15, p. eaar7555, 2018.
- [19] W. Mosauer, "On the locomotion of snakes," *Science*, vol. 76, no. 1982, pp. 583–585, 1932.
- [20] H. C. Astley, C. Gong, J. Dai, M. Travers, M. M. Serrano, P. A. Vela, H. Choset, J. R. Mendelson III, D. L. Hu, and D. I. Goldman, "Modulation of orthogonal body enables high maneuverability in sidewinding locomotion," *Proceedings of the National Academy of Sciences*, vol. 112, no. 19, pp. 6200–6205, 2015.
- [21] B. C. Jayne, "What defines different modes of snake locomotion?" *Integrative and Comparative Biology*, vol. 60, no. 1, pp. 156–170, 2020.
- [22] C. Li, T. Zhang, and D. I. Goldman, "A terradynamics of legged locomotion on granular media," *science*, vol. 339, no. 6126, pp. 1408–1412, 2013.
- [23] L. Huang, J. Zhu, Y. Yuan, and Y. Yin, "A dynamic resistive force model for designing mobile robot in granular media," *IEEE Robotics and Automation Letters*, vol. 7, no. 2, pp. 5357–5364, 2022.
- [24] M. G. Bekker, "Introduction to terrain-vehicle systems. part i: The terrain. part ii: The vehicle," Michigan Univ Ann Arbor, Tech. Rep., 1969.
- [25] J.-Y. Wong and A. Reece, "Prediction of rigid wheel performance based on the analysis of soil-wheel stresses part i. performance of driven rigid wheels," *Journal of Terramechanics*, vol. 4, no. 1, pp. 81–98, 1967.
- [26] D. Goldman, H. Komsuoglu, and D. Koditschek, "March of the sandbots," *IEEE Spectrum*, vol. 46, no. 4, pp. 30–35, 2009.
- [27] L. Ding, H. Gao, Z. Deng, J. Song, Y. Liu, G. Liu, and K. Iagnemma, "Foot-terrain interaction mechanics for legged robots: Modeling and experimental validation," *The International Journal of Robotics Research*, vol. 32, no. 13, pp. 1585–1606, 2013.
- [28] R. D. Maladen, Y. Ding, C. Li, and D. I. Goldman, "Undulatory swimming in sand: subsurface locomotion of the sandfish lizard," *science*, vol. 325, no. 5938, pp. 314–318, 2009.
- [29] H. Suzuki, K. Katsushima, and S. Ozaki, "Study on applicability of rft to traveling analysis of wheel with grousers: Comparison with dem analysis as a virtual test," *Journal of Terramechanics*, vol. 83, pp. 15–24, 2019.
- [30] A. Thoesen, S. Ramirez, and H. Marvi, "Screw-powered propulsion in granular media: An experimental and computational study," in *2018 IEEE International Conference on Robotics and Automation (ICRA)*. IEEE, 2018, pp. 4283–4288.
- [31] S. Ozaki and W. Kondo, "Finite element analysis of tire traveling performance using anisotropic frictional interaction model," *Journal of Terramechanics*, vol. 64, pp. 1–9, 2016.
- [32] D. Sulsky, Z. Chen, and H. L. Schreyer, "A particle method for history-dependent materials," *Computer methods in applied mechanics and engineering*, vol. 118, no. 1-2, pp. 179–196, 1994.
- [33] A. Stomakhin, C. Schroeder, L. Chai, J. Teran, and A. Selle, "A material point method for snow simulation," *ACM Transactions on Graphics (TOG)*, vol. 32, no. 4, pp. 1–10, 2013.
- [34] G. Klár, T. Gast, A. Pradhana, C. Fu, C. Schroeder, C. Jiang, and J. Teran, "Drucker-prager elastoplasticity for sand animation," *ACM Transactions on Graphics (TOG)*, vol. 35, no. 4, pp. 1–12, 2016.
- [35] C. Jiang, C. Schroeder, A. Selle, J. Teran, and A. Stomakhin, "The affine particle-in-cell method," *ACM Transactions on Graphics (TOG)*, vol. 34, no. 4, pp. 1–10, 2015.
- [36] Y. Hu, T.-M. Li, L. Anderson, J. Ragan-Kelley, and F. Durand, "Taichi: a language for high-performance computation on spatially sparse data structures," *ACM Transactions on Graphics (TOG)*, vol. 38, no. 6, p. 201, 2019.
- [37] J. L. Tingle, B. M. Sherman, and T. Garland Jr, "Scaling and relations of morphology with locomotor kinematics in the sidewinder rattlesnake *crotalus cerastes*," *Journal of Experimental Biology*, vol. 225, no. 7, p. jeb243817, 2022.



**Lei Huang** (*Student Member, IEEE*) received the B.S. degree in mechanical design, manufacture, and automation from Nanjing Institute of Aeronautics, Nanjing, China, in 2018. He is currently working toward the D.E. degree in mechatronics with the Research Institute of Robotics, School of Mechanical Engineering, Shanghai Jiao Tong University, Shanghai, China.



**Hengqiang Ming** received the B.S. degree in mechanical design, manufacture, and automation from Shandong University, Jinan, China, in 2020. He is currently working toward the M.S. degree in mechatronics with the Research Institute of Robotics, School of Mechanical Engineering, Shanghai Jiao Tong University, Shanghai, China.



**Yuehong Yin** (*Member, IEEE*) received the B.E. degree in mechanical engineering from the Nanjing Institute of Aeronautics, Nanjing, China, in 1990, and the M.S. and Ph.D. degrees from the Nanjing University of Aeronautics and Astronautics, Nanjing, in 1995 and 1997, respectively. He is currently with the State Key Laboratory of Mechanical System and Vibration, Institute of Robotics, Shanghai Jiao Tong University, Shanghai, China. His research interests include robotics, force control, and fields robots.